Spin Cross-Correlation Experiments in an Electron Entangler

Arunav Bordoloi (✉ bordoloiarunav@gmail.com)

University of Basel   https://orcid.org/0000-0002-4885-0472

Valentina Zannier

NEST, Istituto Nanoscienze-CNR & Scuola Normale Superiore

Lucia Sorba

CNR and Scuola Normale Superiore

Christian Schönenberger

University of Basel   https://orcid.org/0000-0002-5652-460X

Andreas Baumgartner

University of Basel and Swiss Nanoscience Institute

Spin Cross-Correlation Experiments
in an Electron Entangler

Arunav Bordoloi[1,*], Valentina Zannier[2], Lucia Sorba[2], Christian Schönenberger[1,3] & Andreas Baumgartner[1,3,*]

[1] *Department of Physics, University of Basel, Klingelbergstrasse 82, CH-4056 Basel, Switzerland*

[2] *NEST, Istituto Nanoscienze-CNR and Scuola Normale Superiore, Piazza San Silvestro 12, I-56127 Pisa, Italy*

[3] *Swiss Nanoscience Institute, University of Basel, Klingelbergstrasse 82, CH-4056, Basel, Switzerland*

[*] *Corresponding authors: arunav.bordoloi@unibas.ch, andreas.baumgartner@unibas.ch*

Correlations are fundamental in describing many body systems - not only in natural sciences. However, in experiments, correlations are notoriously difficult to assess on the microscopic scale, especially for electron spins. Here, we demonstrate a direct measurement of the spin cross-correlations between the currents of a Cooper pair splitter, an electronic device that emits electrons originating from Cooper pairs in a superconductor. While it is firmly established theoretically that these electron pairs form maximally spin-entangled singlet states with opposite spin projections, no spin correlation experiments have been demonstrated so far. We use ferromagnetic sidegates, compatible with superconducting electronic structures, to individually spin polarize the transmissions of two quantum dots fabricated in the two electronic paths, which act as tunable spin filters. The signals are detected in standard transport

and in highly sensitive transconductance experiments. We find that the spin-cross correlation is negative, compatible with spin singlet emission, and deviates from the ideal value mostly due to a finite overlap of the Zeeman split quantum dot states. Our results demonstrate a new route to perform spin auto- and cross correlation experiments in nanometer scaled electronic devices, especially suitable for those relying on magnetic field sensitive superconducting elements, like unconventional, triplet or topologically non-trivial superconductors, or to perform Bell tests with massive particles, like electrons.

Introduction

Correlations are essential in almost all scientific fields and usually describe a relation between two (or more) observed variables. In modern physics, correlations are often used to characterize exotic quantum states,[1,2] or multi-qubit states in prospective quantum computers.[3] Spin correlations are especially interesting, since many thermodynamic phases in condensed matter are related to the electron spin, for example various magnetic phases.[4–6] However, to directly correlate one electron spin to another, i.e. to measure the so called spin cross-correlation, is still uncharted territory.

One of the most prominent examples of correlated electrons are superconductors, in which a large number of electrons forgo their individual fermionic nature and lower the ground state energy by forming a collective of bosonic electron pairs called Cooper pairs.[7] As a consequence, only an even number of electrons can be added or removed at a time at low energies, with the electron pairs forming spin singlet states. The process of two such electrons tunneling into a normal metal is the well known Andreev reflection.[8] If they are allowed to tunnel into two separate normal contacts,
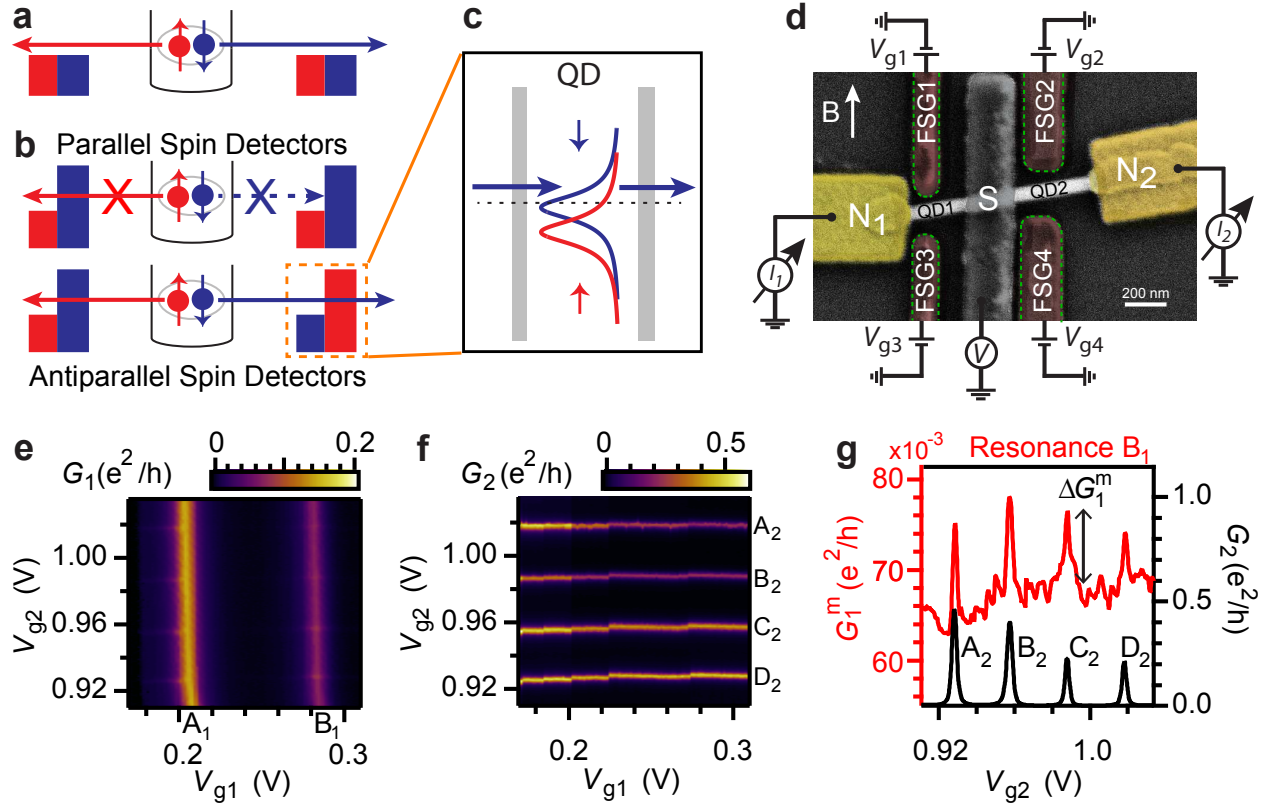
Figure 1: **Principles of spin and charge correlation CPS experiments.** **a** Illustration of the Cooper pair splitting process. **b** Schematic of spin correlation experiments with spin filters to the left and right. **c** Implementation of a spin detector by a Zeeman split quantum dot. **d** False color scanning electron microscopy image of the presented CPS device. **e,f** Differential conductances G_1 and G_2, respectively, measured simultaneously as a function of V_{g1} and V_{g2} at a source-drain bias voltage $V_{dc} = 0$. **g** Conductance maximum G_1^m of QD1 resonance B_1 as a function of gate voltage V_{g2}, showing peaks when G_2 is tuned across the Coulomb blockade resonances A_2-D_2 of QD2.

an additional transport mechanism called crossed Andreev reflection (CAR)[9–11] becomes avail-

able. This process can even become dominating if Coulomb repulsion on small semiconductor islands called quantum dots (QDs) enforce the separation of the charges, which is often called Cooper pair splitting (CPS), and illustrated in figure 1a. Such a device is expected to form a highly efficient source of spatially separated, maximally spin entangled electrons,[12–14] and, more fundamentally, allow for a Bell test with massive particles.[15, 16] The charge correlations in a CPS device, i.e. the simultaneous emission of two electrons, was heavily investigated in recent years, both experimentally,[17–25] and theoretically,[12, 26–29] stressing its fundamental and practical importance.[16, 30–32] However, the experimental detection of the corresponding spin states and their correlations have proven to be very challenging,[33–35] especially since most proposed schemes rely on ferromagnetic contacts competing with superconductivity.

In this work, we directly measure the cross-correlation between the spin currents emitted from a superconductor (S) into two adjacent QDs in a Cooper pair splitter. The basic idea is illustrated in figure 1b. If both contacts to S act as spin filters, i.e. with a spin dependent single electron transmission, the probability for a Cooper pair in the singlet state $|\mathrm{cps}\rangle = \frac{1}{\sqrt{2}}\left(|\uparrow\downarrow\rangle - |\downarrow\uparrow\rangle\right)$ to be split into the two contacts depends on the relative orientation of the spin filters: for fully polarized spin filters oriented in parallel, we expect the probability for Cooper pair splitting to be fully suppressed, while for the anti-parallel orientation CPS is allowed (figure 1b). We use the spin correlation operator $\hat{C} = \sum_{\sigma_1,\sigma_2} s_1 s_2 |\sigma_1\sigma_2\rangle \langle\sigma_1\sigma_2|$ with $\sigma_j \in \{\uparrow,\downarrow\}$, $s_j = +1(-1)$ for $\sigma_j = \uparrow (\downarrow)$, i.e. with a positive value for parallel spins and a negative value for anti-parallel spins, where j labels the QD. For the fully anti-correlated Cooper pair states, the expectation value for $\hat{C}$ should reach $\langle\hat{C}\rangle_{\mathrm{cps}} = -1$. All other possible transport processes[20, 21, 36] are discussed in extended

data table 1 and result in correlation values of either zero for processes involving only one QD, or positive values for higher order two-dot processes. In direct transport and transconductance experiments, we demonstrate a clear negative spin cross-correlation reaching values of $\langle \hat{C} \rangle_{\text{exp}} \approx -0.4$, limited by the polarization of the spin filters. Such devices provide a direct route towards spin correlation experiments at the nanometer scale in modern quantum-electronic devices suitable for various applications, such as the detection of triplet and topological superconductivity,[37,38] the investigation of correlated ferromagnetic phases in van der Waals heterostructures,[6] and mark a first step towards a solid-state Bell test.[16]

A false color scanning electron microscopy (SEM) image of the presented CPS device is shown in figure 1d. An indium arsenide (InAs) nanowire (NW) is contacted in the center by a titanium/aluminium superconducting source contact (S) and at the ends by titanium/gold normal metal contacts (N_1 and N_2), with a QD forming in each of the NW segments in between. Spin filtering is implemented by individually Zeeman splitting the QD resonances by the magnetic stray field that develops in the narrow gap fabricated in a long strip of a ferromagnetic metal (Permalloy), which we call ferromagnetic split-gate (FSG).[39,40] We use the labels $(+,+)$ and $(-,-)$ for the two parallel and $(+,-)$ and $(-,+)$ for the two anti-parallel magnetization states. In the extended data figures 1 and 2, we demonstrate that the stray fields do not suppress superconductivity in the nearby S contact.

For later use, we introduce a spin polarization for each QD:[40] the Zeeman splitting of the QD states results in a spin-dependent single particle transmission (or transmission density of states)

D_σ for the spin state $\sigma \in \{\uparrow, \downarrow\}$,[39–42] as illustrated in figure 1c. We define the spin polarization at the Fermi energy, E_F, for a given QD as

$$P = \left. \frac{D_\uparrow - D_\downarrow}{D_\uparrow + D_\downarrow} \right|_{E=E_\mathrm{F}} \tag{1}$$

which depends on the stray magnetic field B_str, the external magnetic field B and the gate voltage V_g. This polarization directly results in a spin-polarized current through the individual QDs.

First, we establish Cooper pair splitting by demonstrating a positive *charge* current cross-correlation, which corresponds to the simultaneous emission of two electrons from a Cooper pair into the different QDs. As illustrated in figure 1d, we simultaneously measure the two differential conductances $G_j = dI_j/dV$, with I_j the current measured through QD j and V the common bias voltage applied to the superconductor S. The two conductances at zero dc bias and zero external magnetic field are plotted as a function of the FSG gate voltages V_g1 and V_g2 in figures 1e and 1f, respectively. Each QD exhibits Coulomb blockade resonances tuned almost exclusively by the corresponding FSG voltage, suggesting very small cross capacitances to the respective far QD. In the following experiments, we avoid gate regions with parametric charge rearrangements, seen as small shifts in the resonance positions in the large area scans of figure 1f. Transport through one QD is only possible either mediated by Andreev reflection, or by higher order processes, since a double occupancy of the QD is suppressed by Coulomb interactions, and sequential tunneling through the QD by the required generation of a quasi-paricle in the superconductor.[21] In our case the QDs are rather strongly coupled to S, so that the former process seems more probable (see extended data figure 2).
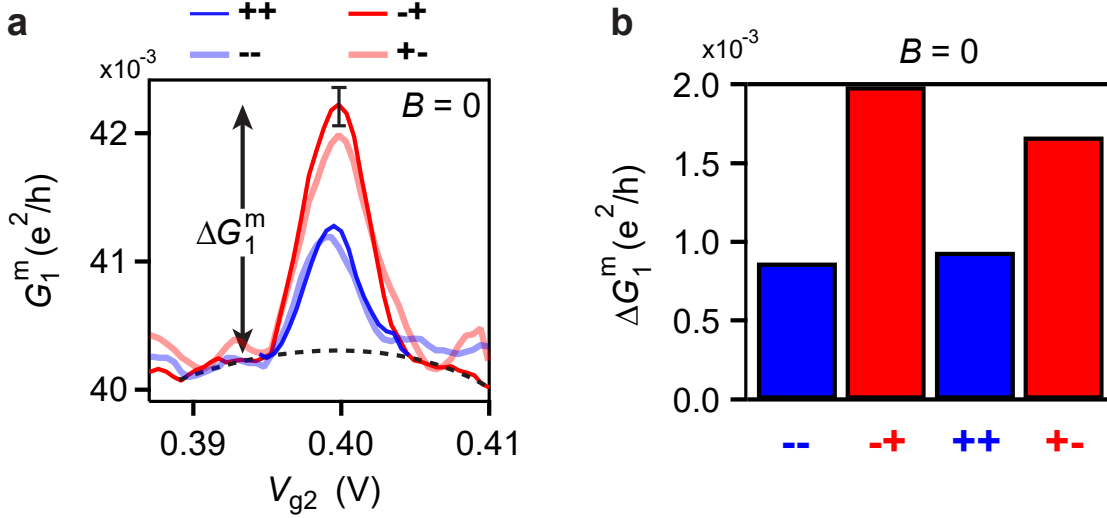
Figure 2: **Spin Correlation Measurements. a** Maximum conductance G_1^m as a function of the gate voltage V_{g2} for all four magnetization states at $B = 0$ and $V_{dc} = 0$ for QD2 resonance R_2, showing a suppression of the conductance for the parallel magnetization states relative to the antiparallel states. The black dotted line shows the background for the state (-,+) subtracted in **b**. **b** Modulation amplitude of the maximum conductance ΔG_1^m for all four magnetization states extracted from **a**.

If both QDs are resonant, i.e. at gate voltages at which a resonance of QD1 'crosses' one of QD2, Cooper pair splitting becomes allowed, and an additional current flows through *both* QDs. This is weakly visible in the large scale data of figure 1e. To see it better, we plot in figure 1g the resonance maximum G_1^m of QD1 resonance B_1 as a function of V_{g2} (red), which tunes QD2 through the resonances A_2 to D_2, as plotted in black. G_1^m shows pronounced peaks whenever QD2 becomes resonant, which can be directly attributed to the CPS process.[17,20,21] To quantify this effect, we measure the modulation amplitude ΔG_1^m, as indicated in figure 1g. Similar data for the other resonance A_1 is shown in extended data figure 3. This amplitude modulation vanishes if the

superconductivity is suppressed by an external magnetic field, as demonstrated in extended data figure 4.

The main step now is to assess the spin correlations. To do this, we measure the charge correlations for the four different spin filter settings, i.e. for the four orientations of the FSGs. The sweep sequence to obtain these magnetization states is described in the Methods. Figure 2a shows the maximum conductance G_1^{m} as a function of V_{g2} for the two parallel and two anti-parallel FSG magnetization orientations at zero external magnetic field, $B = 0$, for the resonances R_1 and R_2 shown in extended data figure 5. For all magnetizations we find a maximum in G_1^{m} at the gate voltage of QD2 resonance R_2, demonstrating that the resonance positions do not change significantly with changes in the stray fields. The main finding is that the maximum conductance for the two parallel orientations is significantly reduced compared to the two anti-parallel orientations. This finding becomes even clearer in figure 2b, where we plot the modulation of the maximum conductance, ΔG_1^{m}, for the four magnetization states. To obtain this value, we individually subtract a parabolic background for each curve, shown as black dashed line for the state $(-, +)$ in figure 2a. Figure 2b directly illustrates that the modulation amplitude is suppressed by a factor of ~ 2 for the two parallel magnetization states with respect to the two anti-parallel states, in qualitative agreement with the negative spin cross-correlation expected for Cooper pair emission.

To discriminate the CPS contribution from other transport processes, we now investigate the conductance amplitude modulation in both arms, for which we first show that $\Delta G_1^{\mathrm{m}} \approx \Delta G_2^{\mathrm{m}}$, as expected for CPS, and that in both arms the conductance maxima are larger for the anti-parallel
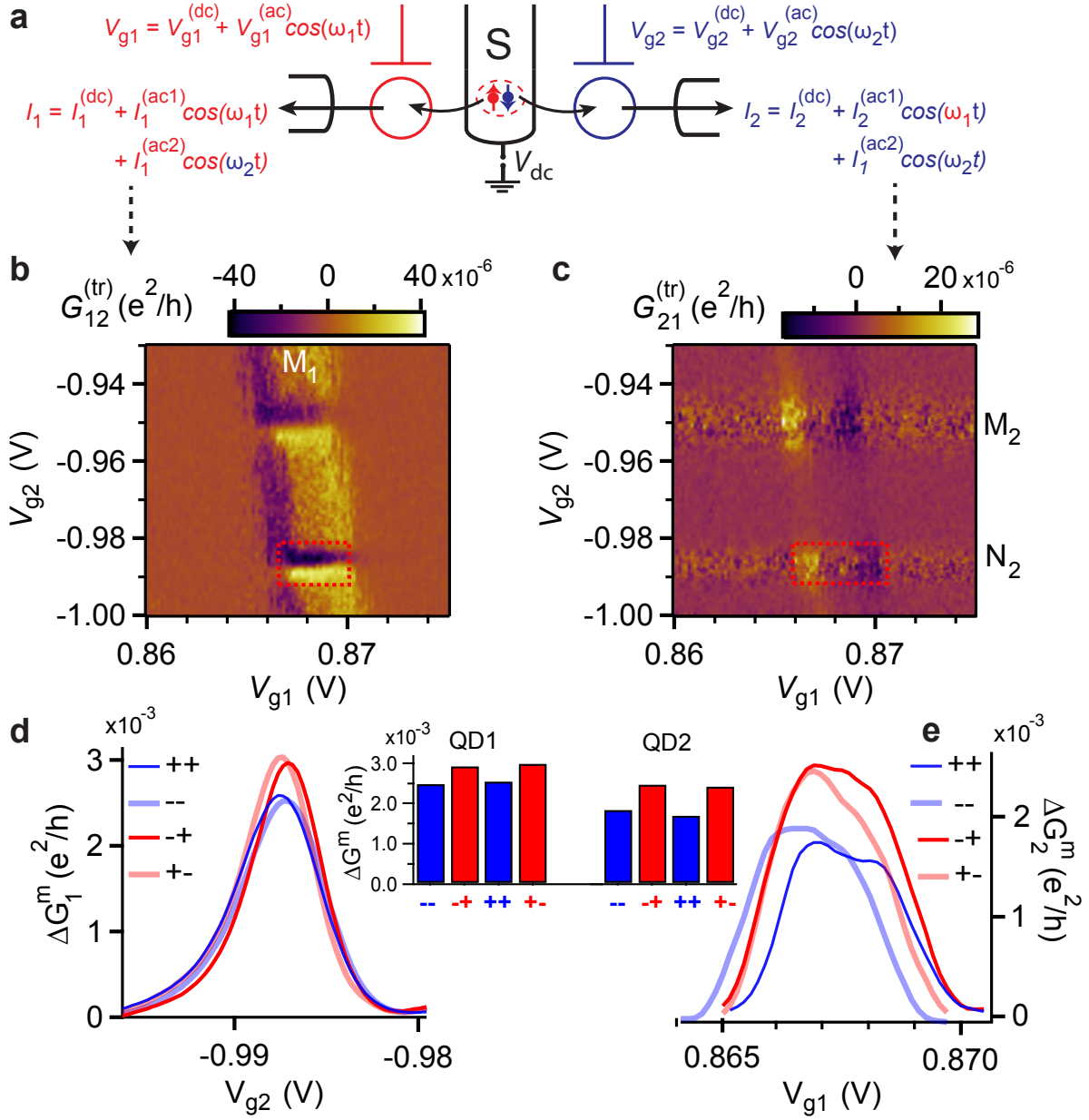
Figure 3: **Transconductance measurements. a** Illustration of the transconductance measurements in a CPS device. **b,c** Transconductance $G_{12}^{(tr)} = \frac{I_1^{(ac2)}}{V_{g2}^{(ac)}}$ and $G_{21}^{(tr)} = \frac{I_2^{(ac1)}}{V_{g1}^{(ac)}}$, respectively, plotted as a function of V_{g1} and V_{g2} for resonance M_1 in QD1 and resonances M_2 and N_2 in QD2 at $B = 0$ for the (+,-) magnetization state. **d,e** Modulation of the maximum conductance ΔG_1^m and ΔG_2^m, respectively, reconstructed from **b** and **c** (see Methods) for all four magnetization states at $B = 0$.

Inset: Bar plot of the maximum conductance modulation ΔG^m for QD1 and QD2 for the four magnetization states.

magnetization configurations than for the parallel, only expected for the CPS mechanism (the spin-dependence of other transport mechanisms is discussed in extended data table 1). In direct experiments as presented above, we can resolve the CPS current only in QD1, but not in QD2, due to the large background conductance. To resolve the CPS currents in both arms, we perform transconductance experiments, as illustrated in figure 3a and described in details in the Methods section. The basic concept is to measure the modulation of the current in one QD upon modulating the gate voltage of the other QD, which is only sensitive to processes in which both QDs are involved.

We thus measure the transconductances $G_{12}^{(\mathrm{tr})} := \frac{dI_1}{dV_{\mathrm{g2}}} = \frac{I_1^{(\mathrm{ac2})}}{V_{\mathrm{g2}}^{(\mathrm{ac})}}$ and $G_{21}^{(\mathrm{tr})} := \frac{dI_2}{dV_{\mathrm{g1}}} = \frac{I_2^{(\mathrm{ac1})}}{V_{\mathrm{g1}}^{(\mathrm{ac})}}$ (with the second step relating to the lock-in detection scheme described in figure 3a and the Methods). Both transconductances are plotted as a function of the gate voltages V_{g1} and V_{g2} in figures 3b and 3c, respectively. Both exhibit peak-valley features at the indicated QD resonances, consistent with maxima in G_1 and G_2 when measured along the respective resonances. The direct integration of these data allows us to reconstruct the modulation of the conductance maxima ΔG_1^{m} and ΔG_2^{m} (details in Methods). The results are plotted in figures 3d and 3e for all four magnetization states at $B = 0$, for the resonance crossings M_1 and N_2 in the gate voltage intervals indicated by the dashed rectangle in figures 3b and 3c, respectively (see extended data figure 6 for details).

The reconstructed conductance modulations are similar as in the previously discussed data set and of similar magnitude for both QDs, in spite of rather different background conductances. With both conductance variations available, we can assess the fraction of CPS in the signals. We

expect a positive variation in both arms only for CPS, so that we take the minimum of both signals as a lower bound for CPS,[20] i.e. $\Delta G^{\text{cps}} = \Delta G_2^{\text{m}}$ as $\Delta G_1^{\text{m}} > \Delta G_2^{\text{m}}$, while the large backgrounds in both signals that depend only on one QD are due to local pair tunneling (LPT), and the remaining part $\Delta G^{\text{other}} = \Delta G_1^{\text{m}} - \Delta G_2^{\text{m}}$ is due to CPS followed by direct cotunneling between the QDs, as discussed in extended data table 1. The fraction of the CPS generated currents in our devices are on a similarly small scale as in previous NW-based experiments, which we express as the efficiency[20] $\eta_{\text{tot}} = \frac{2\Delta G^{\text{cps}}}{G_1^{\text{m}} + G_2^{\text{m}}} \approx 3\%$. However, the CPS fraction in the signals that depend on *both* QDs is very large, namely $\eta_{\text{2dot}} = \frac{\Delta G^{\text{cps}}}{\Delta G^{\text{cps}} + \Delta G^{\text{other}}} \approx 85\%$. This latter number suggests that most of the transconductance is due to CPS.

Most importantly, we again show the maximum modulations for the four magnetization states as bar plots in the shared inset of figures 3d and 3e, demonstrating the *simultaneous* suppression of the signals in both arms for the parallel magnetization states compared to the anti-parallel states, directly illustrating a spin anti-correlation. We show explicitly in the Methods how we extract the expectation value of the spin correlation operator from the experiments. The crucial steps are that we first account for non-ideal QD polarizations, $P_j < 1$, meaning for example that an electron in state $|\uparrow\rangle$ can enter the detector set to the opposite magnetization and would be wrongly detected as a $|\downarrow\rangle$ electron. To do this, we introduce the normalized tunnel probabilities at the Fermi energy $\Gamma_{\uparrow,\downarrow}^i = \frac{D_{\uparrow,\downarrow}}{D_\uparrow + D_\downarrow}\big|_{E=E_F}$ for each spin species and FSG magnetization $i \in \{+, -\}$, such that the non-ideal projection operators is given by $\hat{M}_{\text{nid}}^i = \Gamma_\uparrow^i |\uparrow\rangle \langle\uparrow| + \Gamma_\downarrow^i |\downarrow\rangle \langle\downarrow|$ with $\Gamma_\uparrow^i + \Gamma_\downarrow^i = 1$. With these non-ideal projection operators, we define the non-ideal (nid) spin cross-correlation operator[16]

$$\hat{C}_{\text{nid}} = (\hat{M}_{1,\text{nid}}^+ - \hat{M}_{1,\text{nid}}^-) \otimes (\hat{M}_{2,\text{nid}}^+ - \hat{M}_{2,\text{nid}}^-). \tag{2}$$

For example, the expectation value for ideally split Cooper pairs reads $\langle \text{cps}| \hat{C}_{\text{nid}} |\text{cps}\rangle = -P_1 P_2 < 0$, with P_1 and P_2 the magnitudes of the spin filter polarizations.

Next, we use the tunnel probabilities to express the conductance variations and $\hat{C}_{\text{nid}}$ (see Methods for details), with the intuitive result that we can use the conductance variations in the four magnetization states to estimate the spin correlation in the experiments:

$$\left\langle \hat{C} \right\rangle_{\text{exp}} := \frac{\Delta G^{\text{cps}}_{++} - \Delta G^{\text{cps}}_{+-}}{\Delta G^{\text{cps}}_{++} + \Delta G^{\text{cps}}_{+-}}, \tag{3}$$

where $\Delta G^{\text{cps}}_{++}$ and $\Delta G^{\text{cps}}_{+-}$ are the measured CPS conductance variations. We note that based on the results above, we neglect here non-CPS contributions involving both QDs. For the data set of figure 2b, we find a spin cross-correlation of $\left\langle \hat{C} \right\rangle_{\text{exp}} \approx -0.37$, clearly demonstrating a negative correlation between the spin signals. Assuming that only CPS contributes to the conductance variations, we obtain the geometric mean of the polarizations as $\bar{P} = \sqrt{P_1 P_2} \approx 60\%$ at $B = 0$ and on resonance, similar to values achieved in a double quantum dot spin valve.[40] Similarly, we find for the data in figure 3d and 3e the correlation $\left\langle \hat{C} \right\rangle_{\text{exp}} \sim -0.12$ and $\bar{P} \approx 35\%$, smaller than for the resonances in figure 2, consistent with a reduced mean polarization due to a larger life time broadening of these QD states.[40]

The mean QD polarization and the spin filtering effect of a QD, which consequently influences $\left\langle \hat{C} \right\rangle_{\text{exp}}$, can be further increased by applying a homogeneous external magnetic field, limited by the larger switching field to still be able to access all magnetization states,[40] and by the critical magnetic field of the superconductor. Figures 4a,b show the measured modulation in the conductance maximum ΔG^{m}_1 for the resonances X_1 and X_2 shown in extended data figure 7, with
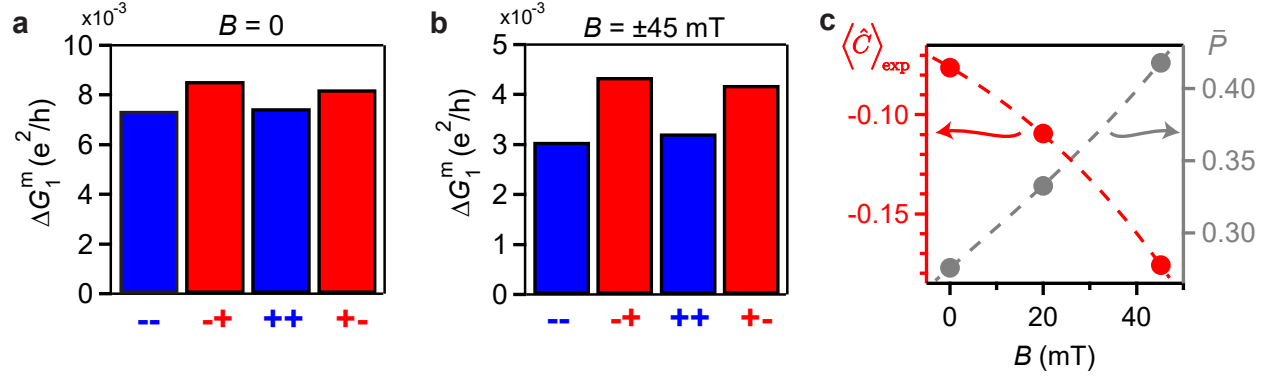
their

Figure 4: **Magnetic field tuning of the QD spin polarization. a,b** Modulation of the conductance maximum ΔG_1^m for all four magnetization states at $B = 0$ and $B = \pm 45\,\mathrm{mT}$, respectively, with the (-,-) and (+,-) configurations measured at $B = -45\,\mathrm{mT}$, and the (+,+) and (-,+) configurations at $B = +45\,\mathrm{mT}$. **c** Experimental spin cross-correlation $\langle \hat{C} \rangle_{\mathrm{exp}}$ (red) and the extracted geometric mean $\bar{P}$ of the QD spin polarizations (grey) as a function of the external magnetic field B, showing a stronger negative correlation for larger QD polarizations.

respective backgrounds subtracted, and for all four magnetization states at $B = 0$ and $B = \pm 45\,\mathrm{mT}$, respectively (CPS signals for $B = \pm 20\,\mathrm{mT}$ can be found in extended data figure 7). ΔG_1^m for the (-,-) and (+,-) states were measured at $B = -45\,\mathrm{mT}$, while the ones for (+, +) and (-,+) were measured at $B = +45\,\mathrm{mT}$, so that the external field boosts the stray field magnitude of the wider, already switched FSG. We again find that the maximum modulations are suppressed for both parallel states with respect to the two anti-parallel states, consistent with a negative spin cross-correlation between the split Cooper pair electrons. We note that all absolute modulation amplitudes ΔG_1^m decrease with increasing B, as does the single QD backgrounds (see extended

data figure 8), qualitatively consistent with local pair tunneling and spin filtering in one QD. For a given B, we extract the expectation value of the spin correlation operator $\langle \hat{C} \rangle_{\mathrm{exp}}$ using equation 3, which is plotted in figure 4c (red symbols). Again assuming an ideal CPS process, we find that the spin cross-correlation becomes stronger and more negative for increasing B, increasing from $\langle \hat{C} \rangle_{\mathrm{exp}} \approx -0.07$ at $B = 0$ to $\langle \hat{C} \rangle_{\mathrm{exp}} \approx -0.17$ at $B = 45\,\mathrm{mT}$, consistent with a larger mean QD spin polarization induced by the additional Zeeman splitting in the external magnetic field. The corresponding mean polarization $\bar{P}$ extracted from $\langle \hat{C} \rangle_{\mathrm{exp}} = -P_1 P_2 = -\bar{P}^2$, is plotted in figure 4c (grey symbols) on the right axis. As one might expect, the mean polarization increases linearly, from $\bar{P} \approx 27\%$ at $B = 0$ to $\bar{P} \approx 42\%$ at $B = 45\,\mathrm{mT}$, consistent with Zeeman split QD states. These polarization values could be improved either by stronger stray fields, for example using other FSG materials like Cobalt, or by increasing the QD lifetime,[43] such that spin cross-correlation experiments with close to ideal anti-correlations $\langle \hat{C} \rangle \approx -1$ become feasible.

As a last step we critically assess one major effect that might influence the spin correlation in our experiments: the FSG stray fields at the position of the superconductor could result in a suppression of the CPS signals. However, even neglecting the Meissner effect preventing magnetic fields from penetrating S, we can expect considerably larger stray fields on S in the anti-parallel states, compared to the parallel ones,[44] which would suppress superconductivity effects like CPS stronger for the anti-parallel configuration, the exact opposite of our findings. As a control, we find that CPS and local pair tunneling are both reduced in a homogeneous external magnetic field (extended data figure 8).

In conclusion, we demonstrate spin correlation experiments in an electron entangler device based on Cooper pair splitting from a superconductor, for which we find a negative value for the spin cross-correlation, $\langle \hat{C} \rangle_{\mathrm{exp}} \approx -0.4 < 0$, as expected for split spin singlet Cooper pairs. In novel transconductance measurements, we find similar magnitudes for the CPS conductances in both arms of the entangler, and a similar suppression of the CPS signals for parallel orientations of the spin filters compared to the anti-parallel, in accordance with Cooper pair splitting. In addition, we report CPS measurements in finite external magnetic fields and demonstrate that the cross correlation signals deviate from the ideal value mainly due to finite QD spin polarizations, not due to spurious transport effects. These findings suggest that in devices with stronger QD confinement, it should be possible to detect the full spin anti-correlation. Our work, general enough to be implemented in any solid-state system with reasonably discrete states, can be used to investigate many fundamental states of matter related to the electron spin, such as topological, unconventional or triplet superconductivity,[30,37,38] equal spin Andreev reflection[45] in hybrid Majorana[46,47] devices, or various correlated ferromagnetic phases, for example in van der Waals heterostructures.[6] Since these entanglers rely on single electron tunneling, they can in principle be operated on the single Cooper pair level,[36,48] ideally suited to perform Bell tests with electron spins.[16,31]

METHODS

Conductance and Transconductance Measurements

The differential conductance for each QD, $G_i = \mathrm{d}I_i/\mathrm{d}V$ with $i = 1, 2$ and $V = V_{\mathrm{dc}} + V_{\mathrm{ac}} \cos(\omega t)$,

were measured simultaneously using standard lock-in techniques with a modulation of the bias voltage of $V_{\mathrm{ac}} = 10\,\mu\mathrm{V}$, at a frequency of 177.77 Hz and at a temperature of $\sim 50\,\mathrm{mK}$.

For the transconductance measurements, we apply a dc voltage of $V_{\mathrm{dc}} = 25\,\mu\mathrm{V}$ to S and measure the variation in the current in one arm that originates from the modulation of the gate voltage of the other arm, which ideally corresponds to the derivative along a QD resonance.

In practice, we modulate the FSG2 voltage on QD2 by an ac voltage $V_{\mathrm{g2}}^{(\mathrm{ac})} = 0.5\,\mathrm{mV}$ at the frequency $\omega_2 = 37.77\,\mathrm{Hz}$ and measure the resulting modulation in the QD1 current, $I_1^{(\mathrm{ac2})}$, at the same frequency ω_2. The resulting transconductance $G_{12}^{(\mathrm{tr})} = \frac{I_1^{(\mathrm{ac2})}}{V_{\mathrm{g2}}^{(\mathrm{ac})}}$ is plotted in figure 3b as a function of the gate voltages V_{g1} and V_{g2}. Similarly, we plot in figure 3c the transconductance $G_{21}^{(\mathrm{tr})} = \frac{I_2^{(\mathrm{ac1})}}{V_{\mathrm{g1}}^{(\mathrm{ac})}}$ that describes the response of the QD2 current to a modulation of $V_{\mathrm{g1}}^{(\mathrm{ac})} = 0.5\,\mathrm{mV}$ in V_{g1} at a frequency $\omega_1 = 77.77\,\mathrm{Hz} \neq \omega_2$.

To reconstruct the the amplitude modulation for each resonance, we first average five cross sections centered on a resonance maximum, as indicated by the red dashed rectangles in figures 3b and 3c. From this curve (not shown), we reconstruct $\Delta G_{1,2}^{\mathrm{m}}$ at the resonance crossing by integrating the transconductance over the voltage on the far gate:

$$\Delta G_j^{\mathrm{m}} = \frac{1}{V_{\mathrm{dc}}} \int_{-\infty}^{V_{\mathrm{g}k}} G_{jk}^{(\mathrm{tr})}(\tilde{V}_{\mathrm{g}k})d\tilde{V}_{\mathrm{g}k}, \tag{4}$$

where j and $k \neq j$ refer to arms 1 and 2, respectively. The obtained modulation of the conductance maxima ΔG_1^{m} and ΔG_2^{m} are plotted in figures 3d and 3e.

Device Fabrication

The InAs NWs were grown by gold (Au) colloid assisted chemical beam epitaxy[49] and have a diameter of 50 ± 5 nm, depending on the size of the gold seed particle. The NWs were mechanically transferred from the growth substrate to a heavily p-doped silicon substrate serving as a global backgate (BG), with a 400 nm SiO_2 insulating top layer. For the electron beam lithography, we employed pre-defined markers and contact pads made of Ti/Au (5 nm/ 45 nm). The normal metal contacts at the NW ends are made of Ti/Au (5 nm/ 45 nm) and the superconducting contact of Ti/Al (5 nm/ 70 nm). Two 5.5 nm wide InP barriers[43] separated by 19 nm InAs below S help to reduce the direct tunnel coupling between the two QD segments. The ferromagnetic split-gates are $6 \, \mu$m long on both sides of the NW and are 100 nm and 180 nm wide, respectively, and made of 30 nm thick Permalloy (Py).[39,40] Before evaporating the normal metal and superconducting contact materials, the native oxide of the NW was etched with a 1:10 ratio $(NH_4)_2S_x : H_2O$ solution for 3.5 minutes. The $(NH_4)_2S_x$ solution was prepared by mixing 0.96 grams of sulfur powder in 10 ml of ammonium sulfide solution (20% in H_2O).

Magnetic Measurements

Each FSG generates a strongly localized stray field, B_{str}, at the corresponding QD position, in the direction of the strip magnetization, which is oriented either parallel or anti-parallel to the long strip axis due to the shape anisotropy.[39,40,50] The FSG magnetization, and with it B_{str}, can be inverted at a characteristic external switching field, B_{sw}, determined by the FSG width in the device design, demonstrated previously using anisotropic magnetoresistance (AMR) measurements[50] as well as spin valve measurements.[40] From independent experiments discussed in extended data figure 9, we

obtain $B_{\text{sw1}} \approx 100\,\text{mT}$ for FSG1 and $B_{\text{sw2}} \approx 25\,\text{mT}$ for FSG2, which allows us to access all four relative FSG magnetization orientations by specific sweep sequences of the external magnetic field B applied along the FSG axes, as discussed below. We label these magnetization states $(+, +)$ and $(-, -)$ for the two parallel and $(+, -)$ and $(-, +)$ for the two anti-parallel configurations.

Spin cross-correlation operator for non-ideal spin detectors

Here, we derive the spin cross-correlation operator for non-ideal spin detectors and the relation to the differential conductances measured in a Cooper pair splitter for the four magnetization states of the ferromagnetic sidegates (FSGs).

In a Cooper pair splitter with *ideal* transmission and *ideal* spin projection operators $M_k^+ = |\uparrow\rangle\langle\uparrow|$ and $M_k^- = |\downarrow\rangle\langle\downarrow|$ in each arm $k \in \{1, 2\}$, the current in one arm is $\propto (M_k^+ + M_k^-)$ and the spin current $\propto (M_k^+ - M_k^-)$. The spin current correlation operator between the two arms thus reads

$$
\begin{aligned}
\hat{C}_{\text{ideal}} &= \left(M_1^+ - M_1^-\right) \otimes \left(M_2^+ - M_2^-\right) \\
&= |\uparrow\uparrow\rangle\langle\uparrow\uparrow| - |\uparrow\downarrow\rangle\langle\uparrow\downarrow| - |\downarrow\uparrow\rangle\langle\downarrow\uparrow| + |\downarrow\downarrow\rangle\langle\downarrow\downarrow|.
\end{aligned}
\tag{5}
$$

For the expectation value of $\hat{C}_{\text{ideal}}$ for Cooper pairs $|\text{cps}\rangle = \frac{1}{\sqrt{2}}[|\uparrow\downarrow\rangle - |\downarrow\uparrow\rangle]$ emitted in the CPS device one directly finds

$$
\langle\text{cps}| \hat{C}_{\text{ideal}} |\text{cps}\rangle = -1,
\tag{6}
$$

while for uncorrelated electrons $\left\langle \hat{C}_{\text{ideal}} \right\rangle = 0$.

To account for *non-ideal* spin detectors and transmissions, we define the spin polarization of a spin

filter - in our case a QD - at the Fermi energy E_F as

$$P = \frac{D_\uparrow - D_\downarrow}{D_\uparrow + D_\downarrow}\bigg|_{E=E_\mathrm{F}} \tag{7}$$

with D_σ the QD transmission (or transmission density of states) for spin state $\sigma \in \{\uparrow, \downarrow\}$. For non-ideal spin detectors with $P_j < 1$, an electron in state $|\uparrow\rangle$ can enter the detector set to detect $|\downarrow\rangle$, and thus get wrongly detected as $|\downarrow\rangle$ with non-zero probability. To accommodate such processes, we define the non-ideal measurement operators of a spin detector as[16]

$$\hat{M}_\mathrm{nid}^+ = \Gamma_\uparrow^+ |\uparrow\rangle\langle\uparrow| + \Gamma_\downarrow^+ |\downarrow\rangle\langle\downarrow|$$
$$\hat{M}_\mathrm{nid}^- = \Gamma_\uparrow^- |\uparrow\rangle\langle\uparrow| + \Gamma_\downarrow^- |\downarrow\rangle\langle\downarrow|, \tag{8}$$

where +(−) denotes the detector set parallel (antiparallel) to the given quantization axis and $\Gamma_{\uparrow,\downarrow}^j$ is given by

$$\Gamma_{\uparrow,\downarrow}^i = \frac{D_{\uparrow,\downarrow}^i}{D_\uparrow^i + D_\downarrow^i}\bigg|_{E=E_\mathrm{F}} = \frac{D_{\uparrow,\downarrow}^i}{D_\mathrm{tot}^i}\bigg|_{E=E_\mathrm{F}} \tag{9}$$

with $i \in \{+, -\}$ and $\Gamma_\uparrow^i + \Gamma_\downarrow^i = 1$. Using the spin polarization from Eq. 7, we can express $\Gamma_{\uparrow,\downarrow}^i$ as

$$\Gamma_\uparrow^i = \frac{1}{2}(1 + P^i) \text{ and } \Gamma_\downarrow^i = \frac{1}{2}(1 - P^i) \tag{10}$$

with P^i the polarization for this QD in magnetization state i. For example, for fully polarized spin detectors, $P^+ = 1$ and $P^- = -1$, so that $\Gamma_\uparrow^+ = \Gamma_\downarrow^- = 1$ and $\Gamma_\uparrow^- = \Gamma_\downarrow^+ = 0$. From Eq. 8, one then again obtains the ideal spin projection operators $\hat{M}_\mathrm{ideal}^+ = |\uparrow\rangle\langle\uparrow|$ and $\hat{M}_\mathrm{ideal}^- = |\downarrow\rangle\langle\downarrow|$. Similarly using Eq. 8, one obtains the non-ideal spin current operator for a single QD,

$$\hat{M}_\mathrm{nid}^+ - \hat{M}_\mathrm{nid}^- = (\Gamma_\uparrow^+ - \Gamma_\uparrow^-)|\uparrow\rangle\langle\uparrow| + (\Gamma_\downarrow^+ - \Gamma_\downarrow^-)|\downarrow\rangle\langle\downarrow|$$
$$= P(|\uparrow\rangle\langle\uparrow| - |\downarrow\rangle\langle\downarrow|) \tag{11}$$
$$= P(\hat{M}_\mathrm{ideal}^+ - \hat{M}_\mathrm{ideal}^-),$$

where we assume for the second step that the magnitude of the spin polarizations in the spin filter settings are equal, $P^+ = -P^- = P$. Now we can write down the spin current cross correlation operator,

$$
\begin{aligned}
\hat{C}_{\text{nid}} &= (\hat{M}_{1,\text{nid}}^+ - \hat{M}_{1,\text{nid}}^-) \otimes (\hat{M}_{2,\text{nid}}^+ - \hat{M}_{2,\text{nid}}^-) \\
&= P_1(|{\uparrow}\rangle\langle{\uparrow}| - |{\downarrow}\rangle\langle{\downarrow}|) \otimes P_2(|{\uparrow}\rangle\langle{\uparrow}| - |{\downarrow}\rangle\langle{\downarrow}|) \\
&= P_1 P_2(|{\uparrow\uparrow}\rangle\langle{\uparrow\uparrow}| - |{\uparrow\downarrow}\rangle\langle{\uparrow\downarrow}| - |{\downarrow\uparrow}\rangle\langle{\downarrow\uparrow}| + |{\downarrow\downarrow}\rangle\langle{\downarrow\downarrow}|) \\
&= P_1 P_2 \hat{C}_{\text{ideal}}
\end{aligned}
\tag{12}
$$

where $P_k^+ = -P_k^- = P_k$ are the polarization magnitudes of the two spin detectors, QD1 and QD2 in our case.

For illustration, we quickly discuss some simple cases: for a spin singlet CPS state, the expectation value of the non-ideal spin cross-correlation operator is $\langle\text{cps}|\,\hat{C}_{\text{nid}}\,|\text{cps}\rangle = -P_1 P_2 < 0$, illustrating the opposite spins of the split Cooper pair electrons. For fully polarized spin filters, $P_1 = P_2 = 1$, one obtains $\langle\text{cps}|\,\hat{C}_{\text{nid}}\,|\text{cps}\rangle = -1$, i.e. the experiment would show a full spin anti-correlation. This ideal value is reduced by non-ideal polarizations, in spite of the CPS state being fully anti-correlated. This shows that the detector quality is relevant for estimating the correlation value in such experiments.

Another instructive example is the product state $|s\rangle = |{\uparrow\downarrow}\rangle$, which as well yields $\langle{\uparrow\downarrow}|\,\hat{C}_{\text{nid}}\,|{\uparrow\downarrow}\rangle = -P_1 P_2 < 0$, the same as the $|\text{cps}\rangle$ state. In contrast, the product state $|s\rangle = |{\uparrow\uparrow}\rangle$ results in $\langle{\uparrow\uparrow}|\,\hat{C}_{\text{nid}}\,|{\uparrow\uparrow}\rangle = P_1 P_2 > 0$, demonstrating a positive correlation. To discriminate the CPS state from the product state $|{\uparrow\downarrow}\rangle$, one would need to perform additional spin cross-correlation mea-

surements with the quantization axis along the other orthogonal axes $\hat{x}, \hat{y}$, as suggested as a Bell test for electrons.[16,31] For all directions, we expect $\langle \mathrm{cps}| \hat{C}_{\mathrm{nid},\hat{x},\hat{y},\hat{z}} |\mathrm{cps}\rangle = -P_1 P_2$ as before, because the $|\mathrm{cps}\rangle$ singlet state is isotropic. In contrast, the product state results in $\langle \uparrow\downarrow| \hat{C}_{\mathrm{nid},\hat{x}} |\uparrow\downarrow\rangle = \langle \uparrow\downarrow| \hat{C}_{\mathrm{nid},\hat{y}} |\uparrow\downarrow\rangle = 0$. Spin cross-correlation measurements along three orthogonal directions would therefore be sufficient to differentiate the maximally entangled $|\mathrm{cps}\rangle$ state from other non-entangled states. Less stringent entanglement witness operators were proposed in References 16 and 32.

As a last step, we need to find a relation between the measured differential conductances and the expectation value of the correlator. The total conductance through a given arm with spin filter setting $i \in \{+, -\}$ is the sum over the two spin channels, which we separate using the spin projection operators:

$$
\begin{aligned}
\hat{G}^i &= \frac{e^2}{h} \left(D_\uparrow |\uparrow\rangle \langle\uparrow| + D_\downarrow |\downarrow\rangle \langle\downarrow| \right) \\
&= \frac{e^2}{h} D_{\mathrm{tot}} \left(\Gamma^i_\uparrow |\uparrow\rangle \langle\uparrow| + \Gamma^j_\downarrow |\downarrow\rangle \langle\downarrow| \right).
\end{aligned}
\tag{13}
$$

The part of the conductance through one QD that depends on both dots, i.e. the *variation* of the QD resonance maxima in the main text, we describe for simplicity as the product of the individual QD transmissions, which in turn depend on the respective spin filter orientations $i, j \in \{+, -\}$:

$$
\Delta\hat{G}^{ij} = \overbrace{\left(\frac{e^2}{h}\right)^2 D_{\mathrm{tot},1} D_{\mathrm{tot},2}}^{=:K} \left[\Gamma^i_{1\uparrow} |\uparrow\rangle \langle\uparrow| + \Gamma^i_{1\downarrow} |\downarrow\rangle \langle\downarrow| \right] \otimes \left[\Gamma^j_{2\uparrow} |\uparrow\rangle \langle\uparrow| + \Gamma^j_{2\downarrow} |\downarrow\rangle \langle\downarrow| \right]
\tag{14}
$$

$$
= K \left[\Gamma^i_{1\uparrow} \Gamma^j_{2\uparrow} |\uparrow\uparrow\rangle \langle\uparrow\uparrow| + \Gamma^i_{1\uparrow} \Gamma^j_{2\downarrow} |\uparrow\downarrow\rangle \langle\uparrow\downarrow| + \Gamma^i_{1\downarrow} \Gamma^j_{2\uparrow} |\downarrow\uparrow\rangle \langle\downarrow\uparrow| + \Gamma^i_{1\downarrow} \Gamma^j_{2\downarrow} |\downarrow\downarrow\rangle \langle\downarrow\downarrow| \right].
$$

We now combine these conductance variations into an expression containing the correlation oper-

ator,

$$\Delta \hat{G}^{++} - \Delta \hat{G}^{+-} - \Delta \hat{G}^{-+} + \Delta \hat{G}^{--} = K \cdot P_1 P_2 \left[|\uparrow\uparrow\rangle \langle\uparrow\uparrow| - |\uparrow\downarrow\rangle \langle\uparrow\downarrow| - |\downarrow\uparrow\rangle \langle\downarrow\uparrow| + |\downarrow\downarrow\rangle \langle\downarrow\downarrow| \right]$$

$$\equiv K \hat{C}_{\text{nid}}.$$

(15)

This combination of the conductance variations in the four magnetization states is therefore a measure for the spin cross-correlation. To account for the prefactor K, we also calculate the following combination:

$$\Delta \hat{G}^{++} + \Delta \hat{G}^{+-} + \Delta \hat{G}^{-+} + \Delta \hat{G}^{--} = K \underbrace{\left[|\uparrow\uparrow\rangle \langle\uparrow\uparrow| + |\uparrow\downarrow\rangle \langle\uparrow\downarrow| + |\downarrow\uparrow\rangle \langle\downarrow\uparrow| + |\downarrow\downarrow\rangle \langle\downarrow\downarrow| \right]}_{=\,1} = K,$$

(16)

independent of the QD polarizations. Dividing equation 15 by equation 16 and replacing each term by its expectation value, we obtain

$$\left\langle \hat{C}_{\text{nid}} \right\rangle = \frac{\Delta G^{++} - \Delta G^{+-} - \Delta G^{-+} + \Delta G^{--}}{G_{++} + \Delta G^{+-} + \Delta G^{-+} + \Delta G^{--}} \approx \frac{\Delta G^{++} - \Delta G^{+-}}{\Delta G_{++} + \Delta G_{+-}}, \qquad (17)$$

where in the last step we assume $\Delta G^{++} \approx \Delta G^{--}$ and $\Delta G^{+-} \approx \Delta G^{-+}$ because ideally there is no preferred direction. Since in our experiments $\Delta G^{++} - G^{+-} < 0$ and all $\Delta G^{ij} > 0$, the spin currents are anti-correlated, as expected for the Cooper pair splitting process.

Magnetic Field Sweep Sequence

The determination of the switching fields in extended data figure 9 enables us to define the procedure to obtain the four magnetization states at zero external magnetic field $B = 0$. The measurements in the main text were all done in the following order:

1. (-,-): Sweep the external magnetic field to $B = -500\,\text{mT} << -B_{\text{sw1}}$ in order to form a single magnetic domain along the FSG axis in the negative direction, followed by a sweep back to $B = 0$ to obtain the magnetization state $(-, -)$, since neither of the FSG magnetization switched into the positive orientation.

2. (-,+): Continue sweeping from $B = 0$ to $B = +45\,\text{mT} > B_{\text{sw2}}$ (but $< B_{\text{sw1}}$), followed by a sweep back to $B = 0$ to obtain the magnetization state $(-, +)$.

3. (+,+): Sweep to $B = +500\,\text{mT} >> B_{\text{sw1}} > B_{\text{sw2}}$ to get a single magnetic domain along the $+B$ direction for both FSGs, followed by a sweep back to $B = 0$ to obtain $(+, +)$.

4. (+,-): Continue sweeping to $B = -45\,\text{mT} < -B_{\text{sw2}}$ (but $> -B_{\text{sw1}}$) followed by a sweep back to $B = 0$ to obtain $(+, -)$.

Similarly, the field sweep sequences used in the experiments for the four magnetization states at $B = \pm 45\,\text{mT}$ in the main text are as follow (similar for $B = \pm 20\,\text{mT}$ in extended data figure 7):

1. (-,-): Sweep the external magnetic field to $B = -500\,\text{mT}$ in order to form a single magnetic domain along the FSG axis, followed by a sweep back to $B = -45\,\text{mT}$ to obtain the magnetization state $(-, -)$ at $B = -45\,\text{mT}$.

2. (-,+): Sweep to $B = +45\,\text{mT}$ to obtain the magnetization state $(-, +)$ at $B = +45\,\text{mT}$.

3. (+,+): Continue sweeping to $B = +500\,\text{mT}$ to get a single magnetic domain along the $+B$ direction, followed by a sweep back to $B = +45\,\text{mT}$ to obtain the $(+, +)$ at $B = +45\,\text{mT}$.

4. (+,-): Continue sweeping to $B = -45\,\mathrm{mT}$ to obtain $(+,-)$ at $B = -45\,\mathrm{mT}$.

Data Availability Statement

References

1. Sachdev, S. Quantum magnetism and criticality. *Nature Physics* **4**, 173–185 (2008).

2. Broholm, C. *et al.* Quantum spin liquids. *Science* **367** (2020).

3. Chatterjee, A. *et al.* Semiconductor qubits in practice. *Nature Reviews Physics* **3**, 157–177 (2021).

4. Fert, A., Reyren, N. & Cros, V. Magnetic skyrmions: advances in physics and potential applications. *Nature Reviews Materials* **2** (2017).

5. Coronado, E. Molecular magnetism: from chemical design to spin control in molecules, materials and devices. *Nature Reviews Materials* **5**, 87–104 (2019).

6. Kurebayashi, H., Garcia, J. H., Khan, S., Sinova, J. & Roche, S. Magnetism, symmetry and spin transport in van der waals layered systems. *Nature Reviews Physics* (2022).

7. Bardeen, J., Cooper, L. N. & Schrieffer, J. R. Theory of superconductivity. *Physical Review* **108**, 1175–1204 (1957).

8. Beenakker, C. W. J. Random-matrix theory of quantum transport. *Reviews of Modern Physics* **69**, 731–808 (1997).

9. Russo, S., Kroug, M., Klapwijk, T. M. & Morpurgo, A. F. Experimental observation of bias-dependent nonlocal andreev reflection. *Physical Review Letters* **95**, 027002 (2005).

10. Cadden-Zimansky, P., Wei, J. & Chandrasekhar, V. Cooper-pair-mediated coherence between two normal metals. *Nature Physics* **5**, 393–397 (2009).

11. Kleine, A., Baumgartner, A., Trbovic, J. & Schönenberger, C. Contact resistance dependence of crossed andreev reflection. *EPL (Europhysics Letters)* **87**, 27011 (2009).

12. Recher, P., Sukhorukov, E. V. & Loss, D. Andreev tunneling, coulomb blockade, and resonant transport of nonlocal spin-entangled electrons. *Physical Review B* **63**, 165314 (2001).

13. Lesovik, G., Martin, T. & Blatter, G. Electronic entanglement in the vicinity of a superconductor. *The European Physical Journal B* **24**, 287–290 (2001).

14. Samuelsson, P., Sukhorukov, E. V. & Büttiker, M. Orbital entanglement and violation of bell inequalities in mesoscopic conductors. *Physical Review Letters* **91**, 157002 (2003).

15. Kawabata, S. Test of bell's inequality using the spin filter effect in ferromagnetic semiconductor microstructures. *Journal of the Physical Society of Japan* **70**, 1210–1213 (2001).

16. Kłobus, W. *et al.* Entanglement witnessing and quantum cryptography with nonideal ferromagnetic detectors. *Physical Review B* **89**, 125404 (2014).

17. Hofstetter, L., Csonka, S., Nygård, J. & Schönenberger, C. Cooper pair splitter realized in a two-quantum-dot y-junction. *Nature* **461**, 960–963 (2009).

18. Herrmann, L. G. *et al.* Carbon nanotubes as cooper-pair beam splitters. *Physical Review Letters* **104**, 026801 (2010).

19. Das, A. *et al.* High-efficiency cooper pair splitting demonstrated by two-particle conductance resonance and positive noise cross-correlation. *Nature Communications* **3** (2012).

20. Schindele, J., Baumgartner, A. & Schönenberger, C. Near-unity cooper pair splitting efficiency. *Physical Review Letters* **109**, 157002 (2012).

21. Fülöp, G. *et al.* Local electrical tuning of the nonlocal signals in a cooper pair splitter. *Physical Review B* **90**, 235412 (2014).

22. Tan, Z. *et al.* Cooper pair splitting by means of graphene quantum dots. *Physical Review Letters* **114**, 096602 (2015).

23. Lee, G.-H. *et al.* Inducing superconducting correlation in quantum hall edge states. *Nature Physics* **13**, 693–698 (2017).

24. Ranni, A., Brange, F., Mannila, E. T., Flindt, C. & Maisi, V. F. Real-time observation of cooper pair splitting showing strong non-local correlations. *Nature Communications* **12** (2021).

25. Pandey, P., Danneau, R. & Beckmann, D. Ballistic graphene cooper pair splitter. *Physical Review Letters* **126**, 147701 (2021).

26. Futterer, D., Governale, M., Pala, M. G. & König, J. Nonlocal andreev transport through an interacting quantum dot. *Physical Review B* **79**, 054505 (2009).

27. Trocha, P. & Weymann, I. Spin-resolved andreev transport through double-quantum-dot cooper pair splitters. *Physical Review B* **91**, 235424 (2015).

28. Trocha, P. & Wrześniewski, K. Cross-correlations in a quantum dot cooper pair splitter with ferromagnetic leads. *Journal of Physics: Condensed Matter* **30**, 305303 (2018).

29. Tam, M., Flindt, C. & Brange, F. Optimal entanglement witness for cooper pair splitters. *Physical Review B* **104**, 245425 (2021).

30. Benjamin, C. Crossed andreev reflection as a probe for the pairing symmetry of ferromagnetic superconductors. *Physical Review B* **74**, 180503 (2006).

31. Braunecker, B., Burset, P. & Yeyati, A. L. Entanglement detection from conductance measurements in carbon nanotube cooper pair splitters. *Physical Review Letters* **111**, 136806 (2013).

32. Busz, P., Tomaszewski, D. & Martinek, J. Spin correlation and entanglement detection in cooper pair splitters by current measurements using magnetic detectors. *Physical Review B* **96**, 064520 (2017).

33. Beckmann, D., Weber, H. B. & v. Löhneysen, H. Evidence for crossed andreev reflection in superconductor-ferromagnet hybrid structures. *Physical Review Letters* **93**, 197003 (2004).

34. Scherübl, Z., Pályi, A. & Csonka, S. Probing individual split cooper pairs using the spin qubit toolkit. *Physical Review B* **89**, 205439 (2014).

35. Hels, M., Braunecker, B., Grove-Rasmussen, K. & Nygård, J. Noncollinear spin-orbit magnetic fields in a carbon nanotube double quantum dot. *Physical Review Letters* **117**, 276802 (2016).

36. Ranni, A. *et al.* Local and non-local two-electron tunneling processes in a cooper pair splitter (2022). arxiv:2201.13109.

37. Bergeret, F. S., Volkov, A. F. & Efetov, K. B. Odd triplet superconductivity and related phenomena in superconductor-ferromagnet structures. *Reviews of Modern Physics* **77**, 1321–1373 (2005).

38. Jeon, K.-R. *et al.* Long-range supercurrents through a chiral non-collinear antiferromagnet in lateral josephson junctions. *Nature Materials* **20**, 1358–1363 (2021).

39. Fábián, G. *et al.* Magnetoresistance engineering and singlet/triplet switching in InAs nanowire quantum dots with ferromagnetic sidegates. *Physical Review B* **94**, 195415 (2016).

40. Bordoloi, A., Zannier, V., Sorba, L., Schönenberger, C. & Baumgartner, A. A double quantum dot spin valve. *Communications Physics* **3** (2020).

41. Desjardins, M. M. *et al.* Synthetic spin–orbit interaction for majorana devices. *Nature Materials* **18**, 1060–1064 (2019).

42. Jiang, Y. *et al.* Hysteretic magnetoresistance in nanowire devices due to stray fields induced by micromagnets. *Nanotechnology* **32**, 095001 (2020).

43. Thomas, F. S. *et al.* Highly symmetric and tunable tunnel couplings in InAs/InP nanowire heterostructure quantum dots. *Nanotechnology* **31**, 135003 (2020).

44. Maurer, L., Gamble, J., Tracy, L., Eley, S. & Lu, T. Designing nanomagnet arrays for topological nanowires in silicon. *Physical Review Applied* **10**, 054071 (2018).

45. He, J. J., Ng, T., Lee, P. A. & Law, K. Selective equal-spin andreev reflections induced by majorana fermions. *Physical Review Letters* **112**, 037001 (2014).

46. Mourik, V. *et al.* Signatures of majorana fermions in hybrid superconductor-semiconductor nanowire devices. *Science* **336**, 1003–1007 (2012).

47. Deng, M. T. *et al.* Majorana bound state in a coupled quantum-dot hybrid-nanowire system. *Science* **354**, 1557–1562 (2016).

48. d'Hollosy, S. *et al.* Gigahertz quantized charge pumping in bottom-gate-defined InAs nanowire quantum dots. *Nano Letters* **15**, 4585–4590 (2015).

49. Gomes, U. P., Ercolani, D., Zannier, V., Beltram, F. & Sorba, L. Controlling the diameter distribution and density of InAs nanowires grown by au-assisted methods. *Semiconductor Science and Technology* **30**, 115012 (2015).

50. Aurich, H. *et al.* Permalloy-based carbon nanotube spin-valve. *Applied Physics Letters* **97**, 153116 (2010).

Author Contributions

A.Bordoloi fabricated the devices, performed the measurements, analyzed and interpreted the data. V.Z. and L.S. have grown the nanowires. A.Baumgartner helped with the measurements, data analysis and interpretation. A.Bordoloi and A.Baumgartner wrote the paper. C.S. and A.Baumgartner initiated and supervised the project. All authors discussed the results and contributed to the manuscript.

Competing Interests

The authors declare no competing interests.

Supplementary Files

This is a list of supplementary files associated with this preprint. Click to download.

- ExtendedData.pdf